The Astronomical Journal, 158:219 (10pp), 2019 December https://doi.org/10.3847/1538-3881/ab4a1a

Phosphorus Abundances in the Hyades and Galactic Disk

Z. G. Maas[1], G. Cescutti[2,3], and C. A. Pilachowski[1]
[1] Indiana University Bloomington, Astronomy Department, 727 East Third Street, Bloomington, IN 47405, USA; zmaas@indiana.edu
[2] INAF, Osservatorio Astronomico di Trieste, Via Tiepolo 11, I-34143 Trieste, Italy
[3] IFPU—Institute for Fundamental Physics of the Universe, via Beirut 2, I-34151, Trieste, Italy
Received 2019 August 9; revised 2019 September 26; accepted 2019 September 29; published 2019 November 6

Abstract

We have measured phosphorus abundances in nine disk stars between $-1 <$ [Fe/H] < -0.5 and in 12 members of the Hyades open cluster using two P I lines at 1.06 μm. High-resolution infrared spectra were obtained using Phoenix on Gemini South and abundances were determined by comparing synthetic spectra to the observations. The average abundance for the dwarf stars in our Hyades sample was $\langle$[P/Fe]$\rangle = -0.01 \pm 0.06$ and $\langle$[P/Fe]$\rangle = 0.03 \pm 0.03$ dex for the three giants. The consistency suggests that abundances derived using the 1.06 μm P I lines are not subjected to temperature- or luminosity-dependent systematic effects at high metallicities. Our [P/Fe] ratios measured in disk stars are consistent with chemical evolution models with P yields increased by a factor of 2.75. We find that [P/O], [P/Mg], [P/Si], and [P/Ti] ratios are consistent with the solar ratio over a range of $-1.0 <$ [Fe/H] < 0.2 with the [P/Si] ratio increasing by ~0.1–0.2 dex at the lowest [Fe/H] ratios. Finally, the evolution of [P/Fe] with age is similar to other α elements, providing evidence that P is produced at the same sites.

Unified Astronomy Thesaurus concepts: Stellar abundances (1577); Milky Way disk (1050); Open star clusters (1160)

Supporting material: machine-readable table

1. Introduction

Phosphorus is an important element for life and the seventeenth most abundance element in the universe. P has one stable isotope (^{31}P) and is thought to be primarily produced from neutron capture on Si isotopes in hydrostatic carbon and neon burning in massive stars (Woosley & Weaver 1995). Type Ia supernovae (SNe) may also produce P (Travaglio et al. 2004; Leung & Nomoto 2018) but are thought to be a less significant source than burning in massive stars. Finally, little to no phosphorus is thought to be produced in AGB stars (Karakas & Lugaro 2016).

Abundance measurements of the odd-Z element phosphorus in stars have grown significantly in number recently and have begun to constrain chemical evolution models of P in the Galaxy. The first chemical evolution study of P I used near-infrared features at 1.06 μm and measured P in ~20 FGK dwarfs (Caffau et al. 2011). Additional abundances measurements in metal-poor stars ($-4 <$ [Fe/H] < -0.2) were performed using P I lines in the UV (Jacobson et al. 2014; Roederer et al. 2014). Comparisons to chemical evolution models for these initial studies found that P is underpredicted by models and yields need to be increased by a factor of 2.75 to match the data (Cescutti et al. 2012; Jacobson et al. 2014). Additionally, the inclusion of hypernova production of P is necessary to match [P/Fe] ratios measured in metal-poor stars (Cescutti et al. 2012; Jacobson et al. 2014).

Targeted surveys with the *Y*-band P I features have confirmed an offset between chemical evolution models and abundance measurements over the $-0.6 <$ [Fe/H] < 0.2 metallicity range (Caffau et al. 2016, 2019; Maas et al. 2017). Additional P abundances have also been measured in individual metal-poor stars (Spite et al. 2017), further constraining P production in the early universe. The Apache Point Observatory Galaxy Evolution Experiment (APOGEE) survey has also measured P (Holtzman et al. 2018), however the P I features in the *H* band are weak, blended with telluric features, and blended with other atomic/molecular features. As a result abundance determinations are difficult and there is significant scatter in measured P abundances from *H*-band features (Holtzman et al. 2018; Jönsson et al. 2018).

P abundances from APOGEE spectra show that the P abundance increases as metallicity decreases (Hawkins et al. 2016). APOGEE data also finds that [P/Fe] ratios in Sagittarius dwarf galaxy stars are lower than disk stars and are consistent with nucleosynthesis in core collapse supernova (CCSNe; Hasselquist et al. 2017). Finally, a difference in [P/Mg] ratios in high [Mg/Fe] and low [Mg/Fe] populations using APOGEE data suggests that P may be produced in Type Ia SNe (Weinberg et al. 2019). In addition to APOGEE, P has also been measured in *H*-band Immersion Grating Infrared Spectrometer (IGRINS) spectra in horizontal branch stars (Afşar et al. 2018). Finally, a mean P abundance of 0.10 ± 0.12 dex was measured in the open cluster NGC 6940 (Böcek Topcu et al. 2019).

To further constrain the nucleosynthesis of P, we have measured abundances in 9 stars between $-1 <$ [Fe/H] < -0.5 and 12 stars in the Hyades open cluster using the P I lines at 1.06 μm in stars. By selecting a targeted sample of metal-poor stars we can compare precise P abundances to chemical evolution models. Comparisons of [P/Fe] and P to various α elements will constrain theoretical predictions of how P is produced. Also, the Hyades open cluster sample provides an opportunity to measure P abundances at the high metallicity range (~[Fe/H] = 0.2 dex) at an age of 625 Myr (Perryman et al. 1998), and to test for systematic effects on abundance as a function of $T_{\rm eff}$.

Details of our sample selection and observations are given in Section 2. Our abundance determination, methodology, and uncertainty calculations are explained in 3. The discussion of our results in the context of chemical evolution and

Table 1
Summary of Phoenix Observations

Identifier	UT Date	J[a] (Mag.)	Spectral[b] Type	S/N
		Field Stars		
HIP 6949	2017 Dec 1	6.133	G8IV/V	210
HIP 7961	2017 Dec 4	6.233	G2/3V	220
HIP 10798	2017 Dec 3	5.056	G8V	200
HIP 14086	2017 Dec 3	4.364	K2V	230
HIP 17147	2017 Dec 1	5.588	F7/8V	330
HIP 30439	2017 Dec 3	6.491	G6V	260
HIP 33324	2017 Dec 4	6.231	G2V	230
HIP 38625	2017 Dec 3	5.972	KOV	70
HIP 44075	2017 Dec 4	4.710	G2V	230
		Hyades Cluster Members		
HIP 15304	2017 Dec 1	6.291	F8	160
HIP 15310	2017 Dec 4	6.639	G0	130
HIP 19793	2017 Dec 3	6.877	G5V	140
HIP 19796	2017 Dec 3	6.128	F8V	280
HIP 20205	2017 Dec 4	1.300	G9.5III	80
HIP 20237	2017 Dec 4	6.395	G0V	180
HIP 20455	2017 Dec 4	1.300	G9.5III	90
HIP 20741	2017 Dec 1	6.893	G2V	110
HIP 20889	2017 Dec 4	1.350	G9.5III	90
HIP 20899	2017 Dec 4	6.696	G2V	160
HIP 21112	2017 Dec 4	6.733	F9V	120
HIP 22422	2017 Dec 4	6.642	F8	110

Notes.
[a] J magnitudes from 2MASS (Skrutskie et al. 2006).
[b] Spectral types from the SIMBAD database.

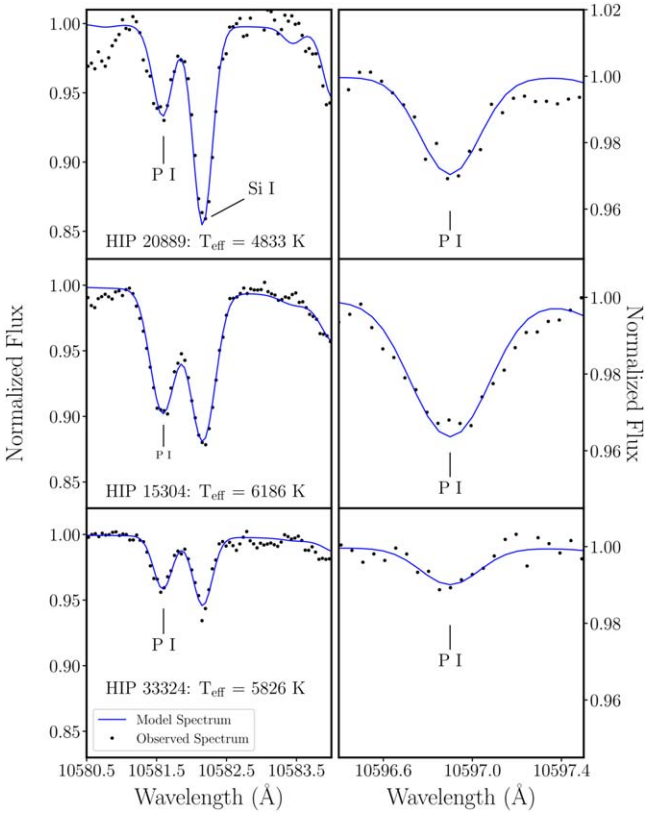

Figure 1. Spectra and synthetic spectra fits to the Hyades giant HIP 20889 (top panel), the Hyades dwarf HIP 15304 (middle panel), and the disk star HIP 33324 (bottom panel). The left column shows fits to the P feature at 10581.5 Å while the right column shows the fit to the weaker P I feature at 10596.9 Å.

nucleosynthesis models is located in Section 4. Finally, our conclusions are summarized in Section 5.

2. Observations and Data Reduction

Observations were performed using Phoenix (Hinkle et al. 1998) on Gemini South as apart of proposal GS-2017B-Q-47. Phoenix is a high-resolution infrared spectrometer capable of observing between 1 and 5μm. We chose the 4 pixel slit width to achieve a resolution of $R \sim 50{,}000$. To observe the P I features at 10581 Å and 10596 Å, we chose a central wavelength of 10593 Å, with a total range of 50 Å. We only selected stars with known atmospheric parameters since the spectral region covered by Phoenix contains too few absorption lines to determine atmospheric parameters independently. We also required sufficiently bright stars ($J \lesssim 7.0$ mag) to achieve the signal-to-noise (S/N) needed to measure weak P I features in our relatively metal-poor stars. We selected our sample stars to measure stars below [Fe/H] < –0.5, where the few existing [P/Fe] abundance measurements are enhanced relative to the solar ratio. The P I features at 1.06 μm however become undetectable at [Fe/H] $\lesssim -1$. We therefore chose stars over the metallicity range of –1 < [Fe/H] < –0.5 from the sample of Bensby et al. (2014), which include both atmospheric parameters and abundance measurements for other elements that would be useful to compare to P. Nine stars in total were observed and the observations are listed in Table 1.

We also included Hyades dwarf and giant stars with homogeneous abundances to probe potential systematic difference in [P/Fe] between low temperature giants and dwarf stars using the P I features at 1.06 μm. We chose the Hyades because several dwarf stars are available at J $\lesssim$ 7.0 mag at a range of atmospheric parameters, three non-binary giants exist in the cluster, and its young age and high metallicity ([Fe/H] = 0.11; Takeda et al. 2013) provide constraints on the younger, more metal-rich stellar population. Spectra were obtained for nine dwarf stars with temperatures ranging from $5735 < T_{\rm eff} < 6291$ K and three giants as shown in Table 1.

Data reduction utilized the IRAF software suite[4] and followed the same procedures described in Maas et al. (2017). To summarize the reduction steps, the images were trimmed, the flat images were dark-subtracted, and flats were median combined. When taking exposures, the objects were nodded along the slit in an "abba" pattern and then subtracted from one another to remove telluric contamination. The object exposures were flat-fielded and extracted, and a wavelength solution was applied to each spectrum. Due to the limited wavelength window, no telluric lines and extremely few standard emission lamp lines were available; the wavelength solution was derived using stellar lines in the region. Finally, the spectra were averaged and normalized. Examples of the two phosphorus features in the final, reduced spectra are shown in Figure 1.

[4] IRAF is distributed by the National Optical Astronomy Observatory, which is operated by the Association of Universities for Research in Astronomy, Inc., under cooperative agreement with the National Science Foundation.

Table 2
Abundance Results

Identifier	$T_{\rm eff}$ (K)	log g	[Fe/H]	ξ (km s^{-1})	$v$sin$i$ (km s^{-1})	References	[Si/Fe]	δ[Si/Fe]	[P/Fe] 10581 Å	δ[P/Fe] 10581 Å	[P/Fe] 10596 Å	δ[P/Fe] 10596 Å
	Field Stars											
HIP 6949	5005	3.35	−0.50	0.96	···	1	0.20	0.03	0.29	0.06	0.38	0.12
HIP 7961	5648	3.91	−0.62	1.08	···	1	0.30	0.03	0.42	0.06	0.33	0.10
HIP 10798	5302	4.61	−0.51	0.65	···	1	0.12	0.05	0.31	0.09	0.22	0.17
HIP 14086	5095	3.47	−0.56	1.03	···	1	0.18	0.03	0.18	0.08	0.14	0.08
HIP 17147	5970	4.52	−0.81	1.27	···	1	0.29	0.03	0.49	0.08	0.47	0.10
HIP 30439	5353	3.79	−0.57	0.85	···	1	0.19	0.06	0.31	0.03	0.31	0.09
HIP 33324	5826	4.24	−0.68	1.12	···	1	0.27	0.03	0.28	0.04	0.19	0.06
HIP 38625	5188	4.40	−0.91	0.62	···	1	0.23	0.13	0.52	0.22	···	···
HIP 44075	5937	4.22	−0.90	1.32	···	1	0.29	0.03	0.50	0.05	0.63	0.06
	Hyades Cluster Members											
HIP 15304	6079	4.45	0.26	1.3	5.5	2	0.01	0.04	0.05	0.07	0.03	0.06
HIP 15310	5894	4.48	0.25	1.1	6	2	0.05	0.03	0.05	0.08	0.10	0.18
HIP 19793	5757	4.51	0.16	1.0	5.5	2	−0.06	0.04	−0.12	0.08	0.04	0.09
HIP 19796	6291	4.40	0.14	1.5	13.4	2	−0.05	0.06	−0.06	0.08	−0.05	0.09
HIP 20205	4875	2.71	0.11	1.43	···	3	0.03	0.06	0.04	0.10	0.01	0.09
HIP 20237	6107	4.44	0.19	1.3	8.9	2	−0.07	0.04	−0.08	0.08	−0.06	0.05
HIP 20455	4816	2.55	0.08	1.35	···	3	0.04	0.05	0.05	0.09	0.18	0.09
HIP 20741	5735	4.51	0.19	1.0	4.3	2	−0.05	0.03	−0.01	0.09	0.07	0.08
HIP 20889	4833	2.74	0.17	1.41	···	3	−0.01	0.06	−0.01	0.10	0.06	0.08
HIP 20899	5924	4.47	0.11	1.1	6	2	0.01	0.03	0.00	0.07	0.25	0.10
HIP 21112	6186	4.42	0.14	1.4	4.9	2	0.06	0.04	−0.02	0.06	0.06	0.06
HIP 22422	6037	4.45	0.16	1.2	5.2	2	0.03	0.04	0.06	0.08	0.00	0.06

Note. Sources: (1) Bensby et al. (2014), (2) Takeda et al. (2013), (3) Dutra-Ferreira et al. (2016). Adopted $A(X)|_{\odot}$: A(Si) = 7.51 (Asplund et al. 2009), A(P) = 5.46 (Caffau et al. 2007), A(Fe) = 7.50 (Asplund et al. 2009).

3. Stellar Abundance Measurements

3.1. Abundance Measurement Methodology

As stated in Section 2, atmospheric parameters for our target stars have been derived in previous studies. The disk star sample was studied by Bensby et al. (2014), Hyades dwarfs' atmospheric parameters were obtained from Takeda et al. (2013), and finally Hyades giants were obtained from Dutra-Ferreira et al. (2016). Atmospheric parameters from Takeda et al. (2013) were adopted because they had self-consistently derived temperature, log(g), metallicity, microturbulence, and $v$sin$i$. The atmospheric parameters for these stars are listed in Table 2.

The effective temperatures adopted from the literature and other atmospheric parameters were computed using different methodologies. First, Bensby et al. (2014) derived their atmospheric parameters using equivalent widths from Fe I and Fe II lines. Differences between effective temperatures and surface gravities derived from stars with accurate parallax values were removed using an empirical correction. The analysis from Takeda et al. (2013) determined their effective temperatures and log(g) from the known luminosities and masses of the Hyades stars (derived in de Bruijne et al. 2001). Finally, Dutra-Ferreira et al. (2016) compared temperatures from spectroscopic methods for the entire sample of Hyades stars, the infrared flux method for dwarf stars, and from angular diameters for the giant stars. Using a line list with few blends and excluding lines with potential non-local thermodynamic equilibrium (NLTE) effects, they were able to determine consistent atmospheric parameters and [Fe/H] abundances for both the dwarf and giant stars.

To test that the different atmospheric parameters are consistent, we derive atmospheric parameters for the stars in our sample using Two Micron All Sky Survey (2MASS) photometry (Skrutskie et al. 2006), V-band photometry adopted from the SIMBAD database, and the $T_{\rm eff}$–color relation from González Hernández & Bonifacio (2009). We removed stars with J and K_s uncertainties above 0.20 mags and converted the K magnitudes of the three Hyades giants to the K_s photometric band. We find the average difference between literature effective temperatures of our sample and J–K_s derived effective temperatures is –32 ± 126 K. The V–K_s required a correction of 0.03 mag to remove a systematic offset between the photometric and the literature values. Without the offset, the average difference is –31 ± 70 K and with the offset a value of 9 ± 64 K. In either case, the standard deviation is consistent with literature $T_{\rm eff}$ measurement errors, indicating that both Hyades and disk star effective temperatures are compatible. The constancy of effective temperatures ensures that no systematic offset is likely due to different atmospheric parameter derivation methodologies. We do not determine full independent atmospheric parameters because too few Fe lines exist in our spectral region to independently determine [Fe/H], microturbulence, or $v$sin$i$.

Abundance measurements were carried out using MOOG (Sneden 1973; v. 2017) with MARCS model atmospheres (Gustafsson et al. 2008). Plane–parallel atmospheric models were used for dwarf stars while spherical models were employed for the three Hyades giants in our sample. We used the phosphorus atomic data from Berzinsh et al. (1997), which has been used to determine abundances in Caffau et al. (2007, 2011, 2016, 2019) and Maas et al. (2017). The `emcee`

Table 3
P Uncertainty Averages

Uncertainty Source	Disk Stars (Dex)	Hyades Giants (Dex)	Hyades Dwarfs (Dex)
$T_{\rm eff}$	0.04	0.06	0.04
log(g)	0.03	0.04	0.02
[Fe/H]	0.01	0.01	0.01
ξ	0.01	0.01	0.01
Fit	0.06	0.07	0.05
N in sample	9	9	3

Python package was also used to achieve the best fit between the model and the data (Foreman-Mackey et al. 2013). A log-likelihood function, shown in Equation (1), was used to find the best-fitting synthetic spectrum to the observed absorption features.

$$\log(L) = -0.5\sum \frac{D - \text{synth}(\lambda, A(P), A(\text{Si}))}{(\sigma * f)^2}. + \log\left(\frac{1}{(\sigma * f)^2}\right), \quad (1)$$

In Equation (1), synth is the synthetic spectrum created by MOOG and D represents the observed data. Three parameters are varied when producing the synthetic spectrum: a wavelength shift of λ, and the input abundances of A(P) and A(Si). Finally, f represents deviations from the expected S/N of 100 (initial σ was assumed to be 0.01). For each iteration, a new synthetic spectrum was generated with parameters for λ, A(P), and A(Si). The 14% and 86% values from the posterior distribution were reported as the uncertainty on the fits. The final best fit to the data using this method for three example stars is shown in Figure 1.

The Markov Chain Monte Carlo (MCMC) fitting methodology was tested by repeating abundance measurements for the P I and Si I features at 10581.57 Å and 10582.16 Å on the stars with known P abundance measurements from Maas et al. (2017). Abundances were rederived using the MCMC code and likelihood equation in Equation (1) then compared to the previous χ^2 minimization results. We found an average difference of [Si/Fe] = 0.00 ± 0.05 dex for Si abundance measurements and [P/Fe] = 0.00 ± 0.08 dex in the 19 stars with Phoenix spectra. One star had an anomalous difference of –0.23 dex (the MCMC abundance–Maas et al. (2017) abundance) which may be due to the low S/N of the spectrum for this object (S/N ∼70). HD 163363 was also indicated as an outlier when comparing abundance fits by eye to χ^2 minimization methods in Maas et al. (2017) and without this star the average difference becomes [P/Fe] = 0.01 ± 0.06 dex for phosphorus. The uncertainties associated with the fits to Si and P are consistent with the standard deviation of the average differences found when comparing the samples. For example, the difference of [P/Fe] = 0.00 ± 0.08 for P is similar to the uncertainty on the fit of 0.05–0.07 dex for the MCMC fits in Table 3 and an average uncertainty on the fit of 0.05 dex from Maas et al. (2017).

3.2. Uncertainties

The uncertainty on each abundance measurement due to noise in the spectra and uncertainty in the atmospheric parameters was calculated, assumed to be independent, added in quadrature, and listed in Table 2. The uncertainty in each abundance measurement due to uncertainty in each atmospheric parameter was derived using new atmospheric models varied by 1σ for a particular atmospheric parameter, then new abundances were derived by fitting the new synthetic spectra to the observed spectra. For each model, one parameter was varied 1σ (e.g., $T_{\rm eff}$) while the others were held constant to the values listed in Table 2.

A grid of synthetic spectra were derived in steps of either 0.01 dex in P or Si abundance, and the best-fitting abundances were found by minimizing the χ^2 between the model fit and the synthetic spectra. The 1σ uncertainties on the atmospheric parameters were adopted from atmospheric parameter sources of Takeda et al. (2013), Bensby et al. (2014), and Dutra-Ferreira et al. (2016) with individual star reference assignments listed in Table 2. As stated in Section 3.1, the uncertainties on the fit were the 14% and 86% values derived from the MCMC fitting methodology. Each uncertainty was added in quadrature and the average uncertainties for each star are included with the results shown in Table 3.

3.3. Examining Systematic Uncertainties in P Abundances

3.3.1. P Abundance Comparison between both P I Features

Our Hyades sample provides a set of chemically homogeneous stars suitable to test if both P I lines give consistent P abundances and if significant systematic effects are present with our 1D LTE methodology. First, we compare the abundances of the 10581 Å and the 10596 Å P I features. Differences in abundance between the lines may indicate an unknown systematic effect on one or both lines, such as blends with other weak absorption features. Abundances from both P I lines in each star in our sample are compared in Figure 2. We find that the average difference between between the two P I lines (in the order of 10581 Å–10596 Å) is Δ[P/Fe] = –0.03 ± 0.09 dex. The average uncertainty for the 10581 Å feature for each stellar population is given in Table 3 at a typical value of 0.06 dex and the average value for the 10596 Å feature is 0.06 dex. Added in quadrature results in a fit uncertainty of 0.08 dex, consistent with the standard deviation of the average differences of the abundance determinations from the two features. Since two lines are not sufficient to do a statistical analysis (e.g., Fe I lines) and averaging the two lines will not lower systematic uncertainties (e.g., from the atmospheric parameters), the results discussed further will use the 10581 Å abundances as these lines are stronger with lower or comparable uncertainties, especially for the disk sample of stars observed which have weak 10596 Å features (as seen in Figure 1).

3.3.2. P Abundances versus T_{eff}

The P I lines used in the abundance analysis have high excitation potentials, slightly below 7 ev (Berzinsh et al. 1997). Although the excitation potential is high, the atomic transitions for these lines are similar to S I lines that show no strong NLTE effects (Asplund et al. 2009). No study has been performed to test for potential NLTE effects on phosphorus abundance derivations using the P I lines. To quantify the potential NLTE effects on measured P abundance empirically, we examine if a relationship exists between effective temperature (and

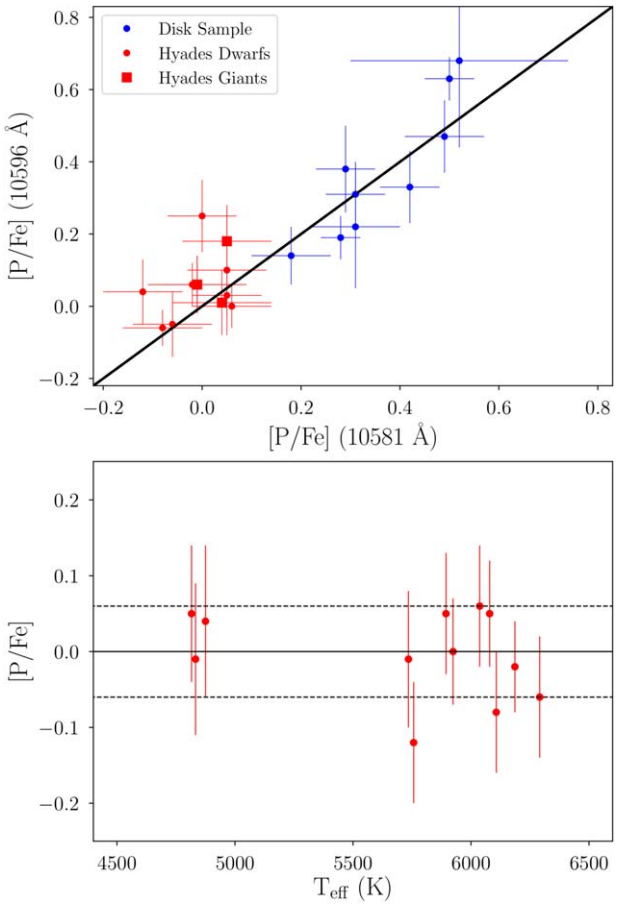

Figure 2. Blue points represent the disk sample of stars with atmospheric parameters from Bensby et al. (2014), red points are Hyades dwarfs, and red squares are Hyades giants. Top panel: comparisons of P abundances derived from the 10581 Å P I lines to the 10596 Å line. The solid black line demonstrates a line with a slope of one. Bottom panel: [P/Fe] ratio against effective temperature. Abundances from the 10581 Å are plotted. Solid lines represents the cluster mean [P/Fe] ratio of 0.00 and dashed lines represent the standard deviation of $\sigma_{[P/Fe]} = 0.06$ dex.

luminosity between dwarfs and giants) and P abundance measurements in our Hyades sample of stars.

We took the average abundance for the nine Hyades dwarfs in our sample, which span in 5735 K $< T_{eff} <$ 6291 K, and compared that to the average of the three Hyades giants ($T_{eff} \sim$ 4800 K). We found the average abundance of the dwarf stars is –0.01 ± 0.06 dex and for the giants is 0.03 ± 0.03 dex (the standard deviation for the sample of stars is quoted as the uncertainty). Additionally, the abundances for each P I feature versus T_{eff} is plotted in the bottom panel of Figure 2. For both lines, no significant dependence between effective temperature and abundance is found.

4. Discussion

4.1. Galactic Chemical Evolution of Phosphorus in the Disk

To augment previous studies on the chemical evolution of P, we have compared our [P/Fe] results to models from Cescutti et al. (2012), Ritter et al. (2018), and Prantzos et al. (2018) along with previous P abundance measurements, shown in Figure 3. Our measurements in disk stars from –1 < [Fe/H] < –0.5 in particular help distinguish between chemical evolution models. The observed [P/Fe] ratios from our chemical evolution model with yields increased by 2.75 from Cescutti et al. (2012; original yields from Kobayashi et al. 2011) fit the results from our new sample with [Fe/H] < –0.5 as well as previous P abundance measurements. The difference between the model and stellar abundances therefore follows the same metallicity dependence as the predicted chemical evolution model (the model slope), which constrains the potential mechanisms needed to enhance P abundances in the chemical evolution models. Possibly the neutron capture cross-section may need to be revisited or the Caffau et al. (2011) suggested proton capture on Si may need to be considered as a possible P production pathway.

We also compare the chemical evolution model of Prantzos et al. (2018) to our abundances in Figure 3. We find that the chemical evolution model underpredicts [P/Fe] abundances over our metallicity range. This result is consistent with the result obtained by the Cescutti et al. (2012) models that adopted the Kobayashi et al. (2011) yields for massive stars without applying any empirical enhancement. When arbitrarily enhanced by a factor of +0.40 dex, we still find that the slope underpredicts the abundances near solar metallicity and underpredicts [P/Fe] ratios for stars with [Fe/H] ∼−1. We note that adopting yields from the stellar model with higher rotation velocity from the set of yields by Limongi & Chieffi (2018; on which the Prantzos et al. (2018) yield is based) will possibly improve the comparison with the data of [P/Fe]. However, this will degrade the fit obtained for many other elements, in particular nitrogen, as described in Prantzos et al. (2018).

Another chemical evolution study by Ritter et al. (2018) found that varying the degree for which the carbon and oxygen shells in massive stars interact or merge increases the yields of the odd-Z elements, such as P. Four chemical evolution models were created by Ritter et al. (2018) with varying C–O shell merger percentages of 0%, 10%, 50%, and 100%. These models are compared to our data in Figure 3. Our abundances also demonstrate that the model with no yield enhancement (0%) predicts a [P/Fe] evolution too low for the measured abundances. The closest matching model has an enhancement of 10%, however the model underpredicts [P/Fe] at the lowest metallicities ([Fe/H]−1.0) and overpredicts the [P/Fe] ratio near the solar [Fe/H] abundance. The C–O shell mergers seem able to produce an enhancement in the P production and this is indeed an interesting feature. Nevertheless, the overall trend obtained by the chemical evolution model appears to be inconsistent with the observational [P/Fe] to [Fe/H] relationship. Possibly, a variable ratio of C–O shell merger events as a function of metallicity could reconcile the model with observation, but similar to rotation for the Prantzos et al. (2018) model, this will produce consequences in the prediction of other elements (such as scandium; see Ritter et al. 2018). To summarize, there are hints from the newest theoretical yields indicating that a solution for the phosphorus production problem in massive stars is close, however currently an empirical modification to adopted yields is needed to fit the observational data, as the one adopted in Cescutti et al. (2012) starting from the Kobayashi et al. (2011) yields.

We also note inconsistencies at the high metallicity end, in particular our measurement of the Hyades open cluster and the previous abundance measurements from Caffau et al. (2011, 2019) and Maas et al. (2017) lie above the chemical evolution model. Adjustments to the chemical evolution model,

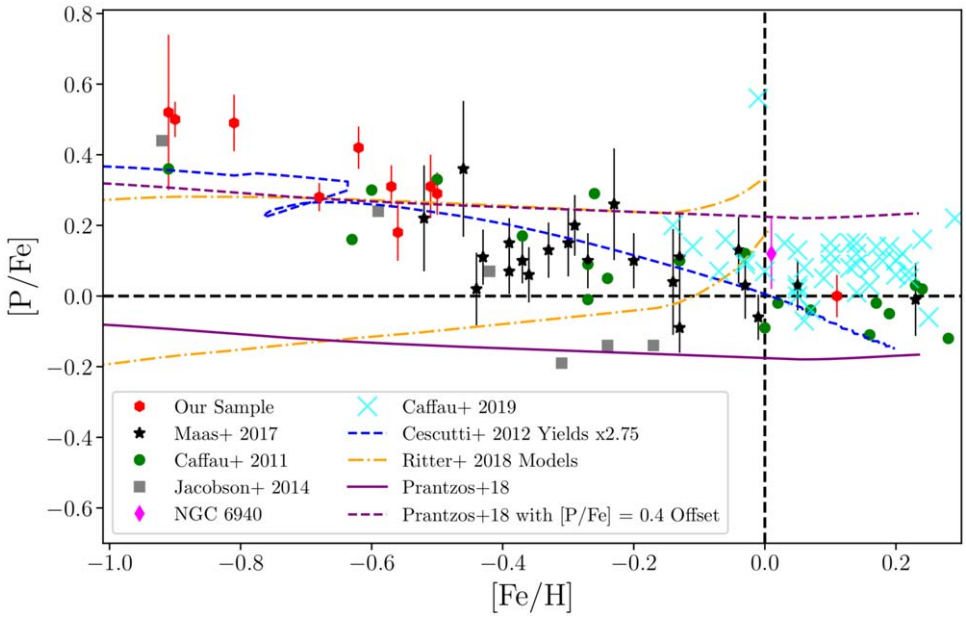

Figure 3. [P/Fe] ratios from this sample (red octagons), Maas et al. (2017; black stars), Caffau et al. (2011; green circles), Jacobson et al. (2014; gray squares), and Caffau et al. (2019; cyan crosses) compared to chemical evolution models. The blue dashed line is a model with the yields increased by a factor of 2.75, from Cescutti et al. (2012). The orange dashed lines are chemical evolution models from Ritter et al. (2018) with O–C shell merger percentages of 0% (model with lowest [P/Fe] ratios predicted) and 10%. The chemical evolution model from Prantzos et al. (2018) is shown as a purple solid line and the model arbitrarily increased by [P/Fe] = 0.4 dex is shown as a purple dashed line. Dashed black lines indicate solar abundances. Red octagon at [Fe/H] = 0.11 represents the average [P/Fe] for the Hyades and the uncertainties represent the standard deviation of the abundance measurements of stars in the cluster. The magenta diamond represents the [P/Fe] cluster average for NGC 6940 (Böcek Topcu et al. 2019).

where an additional production may be needed, or adjustments to the metallicity dependence of SNe yields may be needed to match [P/Fe] ratios at solar metallicity, as shown in Figure 3. One possible solution is P production from a metallicity-dependent source that only produces enough P to be significant at higher metallicities. Böcek Topcu et al. (2019) found a star (MMU 152) in NGC 6940 that exhibited abundance patterns consistent with mass transfer from an AGB star companion (e.g., high N, low C) with a slight P enhancement of ∼0.19 dex relative to the mean value for the other cluster members. However, AGB models do not predict P abundance enhancement (Karakas & Lugaro 2016). P abundance measurements in more metal-rich stars or *s*-process enriched stars may demonstrate whether AGB stars play any role in P production at the high metallicity range.

4.2. Nucleosynthesis of P: Comparisons to Additional Elements

To further explore the nucleosynthesis of P, we compare our P abundances to α elements (O, Mg, Si, and Ti), iron-peak (Ni), and odd-*Z* elements (Al). For the α elements, O and Mg are thought to made almost entirely in hydrostatic burning in massive stars while Si and Ti are predicted to be made significantly in explosive burning in CCSNe with some contributions from Type Ia SNe (Woosley & Weaver 1995; Travaglio et al. 2004). To make these comparisons, we use P and Si abundances in stars from Maas et al. (2017) and this work. Oxygen abundances are adopted from Bensby et al. (2014) for our stars and Ramírez et al. (2013) for the Maas et al. (2017) stars. Additionally, three stars from Caffau et al. (2011) had corresponding oxygen abundances derived by Ramírez et al. (2013). We also adopt Mg, Al, Ti, and Ni abundances from Reddy et al. (2003) for the Maas et al. (2017) stars and from Bensby et al. (2014) for the current sample. Hyades oxygen abundances are obtained from Takeda et al. (2013) while abundances for the other elements are obtained from Carrera & Pancino (2011). Finally, abundances for Arcturus were adopted from Ramírez & Allende Prieto (2011). In all cases, the adopted abundance ratios were rescaled using the solar abundance ratios of Asplund et al. (2009). All abundance ratios are plotted in Figure 4.

From Figure 4 we first note that at the highest metallicity range (–0.5 < [Fe/H] < 0.2) the [P/Si], [P/O], [P/Mg], and [P/Ti] ratios remain consistent with the solar ratio. From –1.0 < [Fe/H] < –0.5, the [P/Si] ratios begin to increase, consistent with a model used in Maas et al. (2017), derived from the P model from Cescutti et al. (2012), Fe yields from Kobayashi et al. (2006), and the Si yields of Woosley & Weaver (1995) and François et al. (2004). The nucleosynthesis prescription adopted for the other elements O, Mg, and Ti is similar to the one adopted in François et al. (2004). We note that the authors assumed empirical modifications—in particular for Mg—to match the trends and the solar abundances of several chemical species (François et al. 2004). Small differences in the Fe yields adopted cause small offsets between the chemical evolution model and the solar abundance ratios. The largest differences was from the [P/O] ratio which was offset by ∼–0.11 dex to normalize the [P/O] ratio to 0 at [Fe/H] = 0. In any case it is quite interesting to find that the [P/Mg] and [P/Ti] are also consistent with chemical evolution models, as shown in Figure 4. Also the [P/O] chemical evolution model is consistent with the observed abundance ratios although there is significant scatter in the observed ratios. Compared to the other observed α elements, oxygen abundances show a dispersion in the data that may be due to the literature [O/Fe] abundances. We also tested [P/Ni] and found a similar behavior to [P/Fe], expected for the iron-peak elements. However, the chemical evolution model

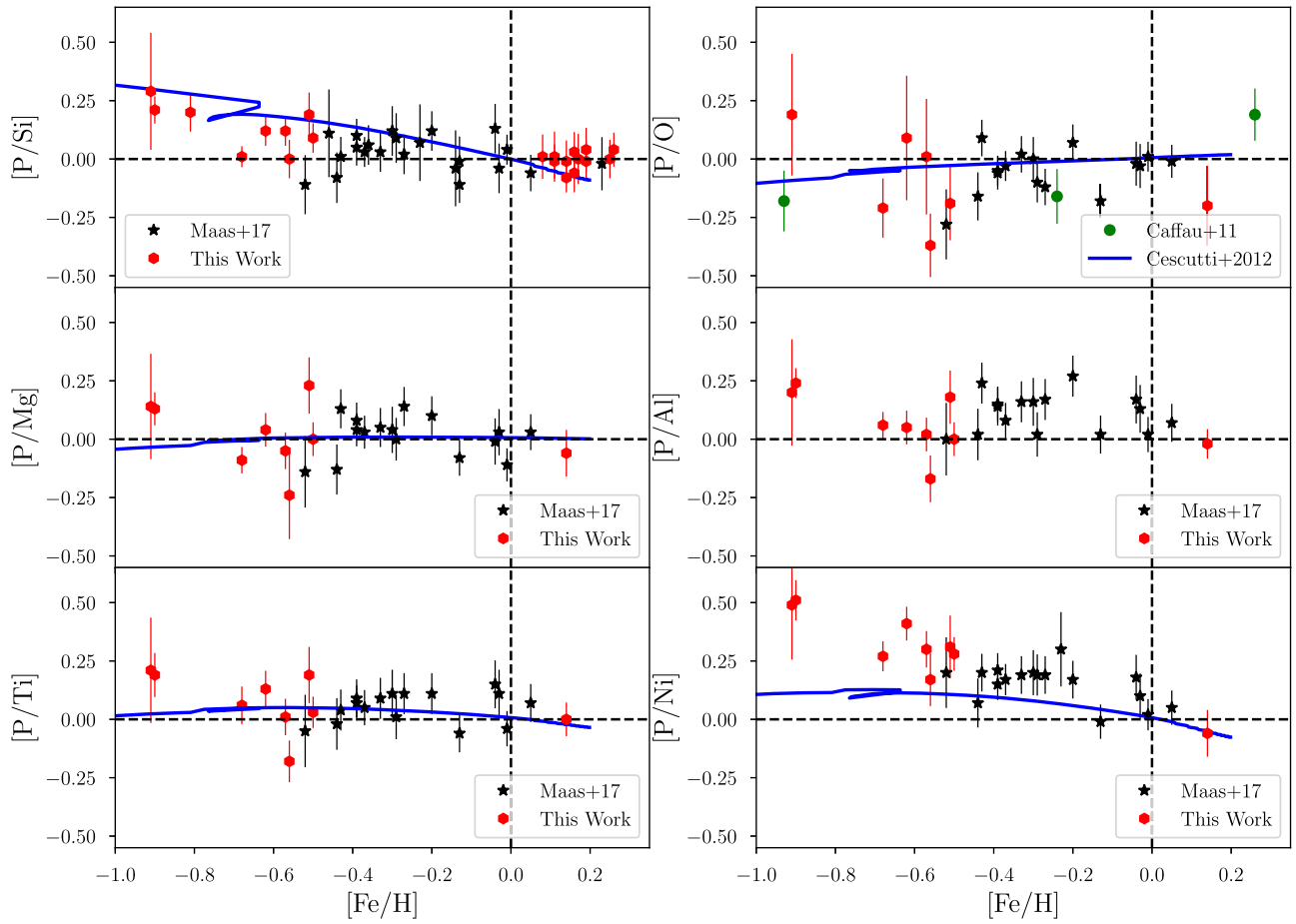

Figure 4. Black stars are measurements from Maas et al. (2017), red hexagons from our sample, and green points from Caffau et al. (2011). Dashed lines represent solar abundances. [P/X] vs. [Fe/H] compared to the chemical evolution models (blue lines).

underpredicts the [P/Ni] at metallicities lower than [Fe/H] < -0.5. A similar slight offset is noticed in Figure 3 and may indicate that metallicity-dependent changes are needed for the empirical P yields. Overall, the nearly solar observed [P/α] ratios and agreement with chemical evolution models suggest that P production is produced in similar environments as the α elements over the metallicity range of $-1 <$ [Fe/H] < 0.

Other odd-Z elements, Na and Al, decrease toward lower metallicities (e.g., the [Na/Mg] and [Al/Mg] ratios in Gehren et al. 2006) as the production method of both relies on neutron density and therefore has strongly metallicity-dependent yields. We tested the [P/Al] abundance and found a slight offset from the solar ratio but consistent [P/Al] ratios at high metallicity. The decrease in neutron density for Al, however, is most significantly observed beyond [Fe/H] < -1 (Gehren et al. 2006). Additionally, the [P/S] ratio was observed to be constant for stars with [Fe/H] $\gtrsim -1.0$ (Caffau et al. 2011) consistent with our α element ratios.

Finally, small or no P contributions from Type Ia SNe are suggested by our [P/α] ratios. While we note a small increase in [P/Si] toward low metallicity, [P/Mg] and [P/Ti] are consistent with the solar ratio over our metallicity range; possibly also [P/O] shows the same trend, although the values for this ratio are scattered, especially at low metallicities. This suggests that small quantities of P are produced in Type Ia SNe, less than than the silicon produced by Type Ia SNe, and compatible with the negligible production of magnesium and oxygen. Studies of multiple APOGEE stars have suggested that P may be significantly produced in Type Ia SNe (Weinberg et al. 2019). However, our [P/Mg] ratios in particular do not suggest that Type Ia SNe are a significant source of P production compared to CCSNe. Additional P abundance measurements in metal-poor disk stars are necessary to confirm these trends.

4.3. Phosphorus Abundances with Age

The stars chosen for this exercise span a large range of ages, from the Hyades at 625 ± 50 Myr (Perryman et al. 1998) to metal-poor thin and thick disk stars from Bensby et al. (2014). We determined ages for stars with known P abundances from Caffau et al. (2011, 2019), Maas et al. (2017), and the stars in this sample. Combining the multiple studies with new measurements from *Gaia* allows us to track the evolution of P with stellar age. Ages were determined from comparisons of the fundamental parameters luminosity, $T_{\rm eff}$, and [Fe/H] to Yonsei-Yale isochrones (Yi et al. 2001). Ages were computed using the $\mathtt{q}^2$ Python package (Ramírez et al. 2014), which adopted a maximum-likelihood method to match the observed stellar parameters to stellar isochrones.

First we compiled parallaxes and *V*-band photometry to measure the luminosity of each star in Caffau et al. (2011, 2019), Maas et al. (2017), and this work. Parallax measurements and their associated uncertainty from the Gaia Data Release 2 (Gaia DR2; Gaia Collaboration et al. 2018) were used to calculate the luminosity. We also adopted Johnson

Table 4
Star Age Estimate

HD Number	[Fe/H] (dex)	δ[Fe/H] (dex)	Age (Gyr)	Age 2σ Lower (Gyr)	Age 2σ Upper (Gyr)	[P/Fe] (dex)	δ[P/Fe] (dex)	[P/Fe] References	U km s^{-1}	V km s^{-1}	W km s^{-1}	P(Thin)	P(Thick)
HIP6949	−0.50	0.05	9.7	6.7	14.5	0.29	0.06	2	43.73	−101.21	34.74	0.00	0.96
HIP7961	−0.62	0.04	12.1	11.2	12.9	0.42	0.06	2	−97.61	−76.08	34.87	0.02	0.94
HIP10306	−0.27	0.15	3.5	2.1	4.2	−0.01	0.03	4	−20.09	−12.22	4.43	0.99	0.01
HIP15675	0.10	0.16	4.4	3.5	4.9	0.09	0.12	1	−51.70	−44.23	13.49	0.90	0.10
HIP17960	0.09	0.17	7.3	2.7	11.3	0.05	0.13	1	10.33	−58.95	−14.74	0.78	0.22

References. (1) Caffau et al. (2019), (2) this Work, (3) Maas et al. (2017), (4) Caffau et al. (2011).

(This table is available in its entirety in machine-readable form.)

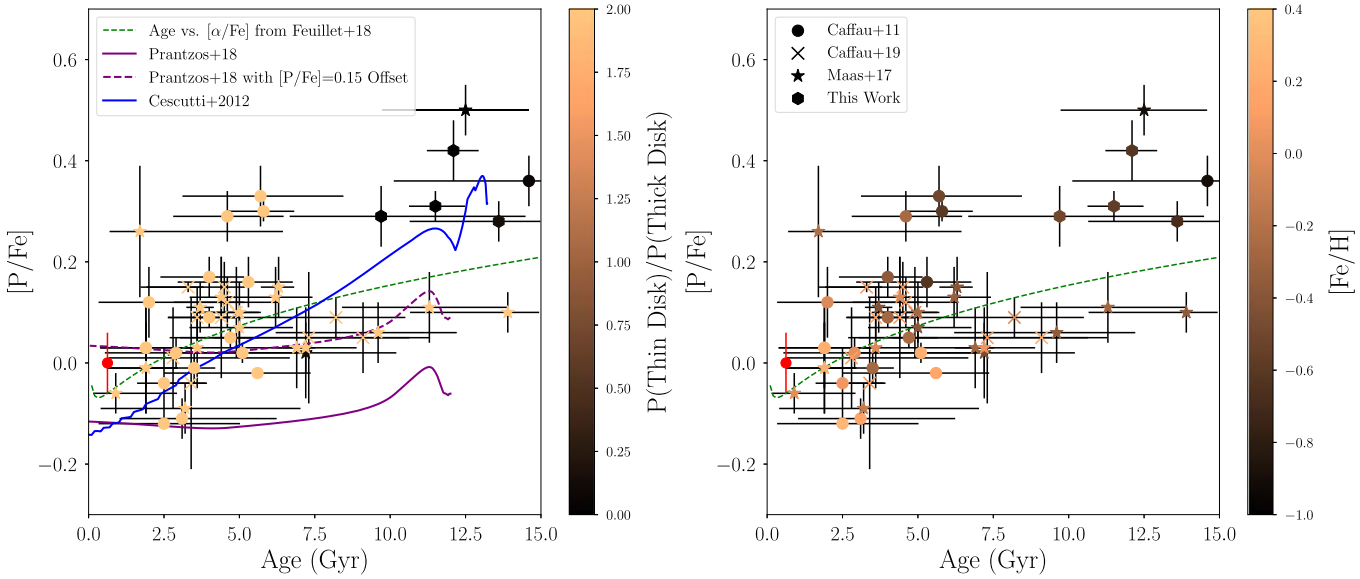

Figure 5. Ages and [P/Fe] ratios from this sample (octagons), Maas et al. (2017; stars), Caffau et al. (2011; circles), and Caffau et al. (2019; crosses). The red octagon represents the average Hyades abundance and the uncertainties represent the standard deviation of the abundance measurements of stars in the cluster. The green dashed line represents the fit to the [α/Fe] trend from Feuillet et al. (2018). Left: color bar shows the thin/thick disk probability ratio. The blue line is a chemical evolution model from Cescutti et al. (2012), while the purple lines are models from Prantzos et al. (2018) Right: color bar represents [Fe/H] for each star.

V-band measurements from the *Hipparcos*/Tycho catalog (ESA 1997), with an assumed uncertainty of 0.01 mags for each measurement. For a few stars, *Gaia* parallaxes or *V*-band magnitudes were not measured. In those cases, *V*-band measurements were adopted from the SIMBAD database and the parallaxes were available from the *Hipparcos* mission (van Leeuwen 2007). Effective temperatures, [Fe/H] abundances, and their uncertainties were adopted from each atmospheric parameter source. In the case of Caffau et al. (2011), effective temperature and metallicity uncertainties were assumed at 100 K and δ[Fe/H] of 0.15 dex. The parameters used and ages calculated are given in Table 4 and the results are plotted in Figure 5. Stars with 2σ uncertainties larger than 5 Gyr were not included since these stars cannot meaningfully constrain phosphorus production over time or distinguish between old populations ($\sim$10 Gyr) and young disk stars.

We also determined thin and thick disk probabilities for the sample stars using phase space information available in the SIMBAD database. The UVW velocities were calculated using a python based UVW calculator.[5] The thin disk, thick disk, and halo membership probabilities based on the UVW velocities were calculated using the same methodology as Ramírez et al. (2013). The UVW velocities and thin/thick disk membership probabilities are included in Table 4.

The compilation of [P/Fe], [Fe/H], thin and thick disk probabilities, and ages are plotted in Figure 5. A clear division in [P/Fe] exists between old (age $\gtrsim$10 Gyr) thick disk stars and the majority of the thin disk stars. Similar offsets for the α elements are observed in older and younger stars (e.g., Bensby et al. 2014; Silva Aguirre et al. 2018). The [P/Fe] ratio in the thin disk stars also appears to decrease slightly from a peak [P/Fe] ratio at $\sim$5 Gyr to the youngest stars at 1 Gyr. However, more accurate ages are necessary to determine the evolution of [P/Fe] in the thin disk stars.

We compare our [P/Fe] and ages to an empirical fit of [α/Fe] versus age in 712 red giant stars observed with APOGEE (Feuillet et al. 2018). The primary metallicity range of the Feuillet et al. (2018) sample is –0.5 < [Fe/H] < 0.4 and their α to age fit reproduced in Figure 5 is consistent with [P/Fe] ratios measured at similar iron abundances. The few metal-poor [P/Fe] measurements are offset at all ages from the empirical fit of Feuillet et al. (2018). As a result, Figure 5 provides additional evidence that P is made in CCSNe and correlates with α elements in stars with similar metallicities.

[5] https://github.com/dr-rodriguez/UVW_Calculator

We also find three high [P/Fe], low metallicity, young thin disk stars, HIP 40843, HIP 51523, and HIP 76716. These three stars are offset from other thin disk stars in Figure 5. The [P/Fe] abundances for these stars were determined by Caffau et al. (2011) and the ages for these stars are confirmed in other studies. HIP 40843 was found to also have an age of 3.39 Gyr, [Fe/H] = –0.26 and [O/Fe] = 0.05 from Ramírez et al. (2013). HIP 51523 was determined to have an [Fe/H] = –0.48 and was classified as a thin disk star by Hinkel et al. (2017). Finally, Holmberg et al. (2009) measured [Fe/H] = −0.11 and an age of 3.1 Gyr for HIP 76716. Errors in age or disk membership cannot explain the high [P/Fe] abundances. Caffau et al. (2011) adopts [Fe/H] = –0.50 for HIP 40843, [Fe/H] = –0.60 for HIP 51523, and [Fe/H] = –0.26 for HIP 76716. Adopting the higher [Fe/H] ratios for these stars in the literature would lower the [P/Fe] ratio by ∼0.12–0.24 dex and would be consistent with other thin disk stars.

Finally, we compared our [P/Fe] ratios and ages to chemical evolution models. We find that the model from Cescutti et al. (2012; blue line in Figure 5) is in general agreement with the thin disk [P/Fe] ratios and thick disk abundances. The chemical evolution model from Prantzos et al. (2018; purple lines in Figure 5) fits only the thin disk stars when enhanced by 0.15 dex. The agreement of the Cescutti et al. (2012) model with age provides additional evidence that the P yields must be offset without changing the metallicity dependence of the empirical yields.

5. Conclusions

We measured P abundances in 21 stars; 9 stars between –1.0 < [Fe/H] < –0.5 and 12 stars in the Hyades open cluster using the 10581 and 10596 Å P I absorption lines. The spectra were obtained with Phoenix on Gemini South and analyzed using MOOG spectral synthesis software. From our abundance measurements we have explored how P is produced in the Galaxy.

1. We found consistent average abundance in nine Hyades dwarf stars (-0.01 ± 0.06) and three Hyades giants (0.03 ± 0.03 dex). Temperature-dependent systematic effects (e.g., NLTE effects) are therefore determined to be small for the P I features observed at this metallicity for FG dwarfs and giants.
2. Our [P/Fe] ratios are consistent with the slope of chemical evolution models but offset over the metallicity range of –1 < [Fe/H] < –0.5. Models with P yields increased by a factor of 2.75 (by [P/Fe] ∼ 0.4 dex) match the chemical evolution models best. New models must therefore increase P production while keeping the same metallicity dependence over –1.0 < [Fe/H] < 0. Additionally, a small increase in P beyond [Fe/H] ∼0 is observed and may be the result of adjustments needed in SNe metallicity-dependent yields and/or contributions from metallicity-dependent P production (e.g., AGB stars) at high metallicities.
3. [P/O], [P/Mg], [P/Al], [P/Si], [P/Ti], and [P/Ni] ratios are compared to chemical evolution models. We find that P ratios to α elements are constant and approximately consistent with the solar ratio over nearly the entire –1.0 < [Fe/H] < 0.2 range, suggesting that P is produced in the same environments as the α elements. We do note that the [P/Si] ratio increases by ∼ 0.1–0.2 dex in the lowest metallicity stars, as expected from models, and suggests that Si is relatively more produced in Type Ia SNe than P. Additionally there are hints that [P/O] decreases at our lowest metallicity range, however because [P/Mg] ∼ 0 over our entire metallicity range, we expect little to no contribution to P from Type Ia SNe.
4. The [P/Fe] trend with stellar age was compared to an empirical [α/Fe] versus age relationship from Feuillet et al. (2018). Our [P/Fe] ratios were consistent with the empirical fit over typical thin disk metallicities demonstrating that P abundances are produced in CCSNe, specifically in the same environments as the α elements. Additionally, low metallicity, probable thick disk stars are offset to higher [P/Fe] ratios than the fit. Finally, our abundances are consistent with the [P/Fe] versus age chemical evolution model from Cescutti et al. (2012).

This work is based on observations obtained at the Gemini Observatory, which is operated by the Association of Universities for Research in Astronomy, Inc., under a cooperative agreement with the NSF on behalf of the Gemini partnership: the National Science Foundation (United States), the National Research Council (Canada), CONICYT (Chile), Ministerio de Ciencia, Tecnología e Innovación Productiva (Argentina), and Ministério da Ciência, Tecnologia e Inovação (Brazil). The Gemini observations were done under proposal ID GS-2017B-Q-47. We thank Steve Margheim for his assistance with the Gemini South Telescope observing run. This research has made use of the NASA Astrophysics Data System Bibliographic Services, the Kurucz atomic line database operated by the Center for Astrophysics. We thank the anonymous referee for the thoughtful comments and suggestions on the manuscript. This research has made use of the SIMBAD database, operated at CDS, Strasbourg, France. This publication makes use of data products from the Two Micron All Sky Survey, which is a joint project of the University of Massachusetts and the Infrared Processing and Analysis Center/California Institute of Technology, funded by the National Aeronautics and Space Administration and the National Science Foundation. We thank Eric Ost for implementing the model atmosphere interpolation code. C.A.P. acknowledges the generosity of the Kirkwood Research Fund at Indiana University. Z.G.M. acknowledges the Indiana University College of Arts and Sciences for research support via a Dissertation Research Fellowship. G.C. acknowledges financial support from the European Union Horizon 2020 research and innovation programme under the Marie Skłodowska-Curie grant agreement No. 664931 and from the EU COST Action CA16117 (ChETEC).

Software: `IRAF` (Tody 1986, 1993), `MOOG` (v2017; Sneden 1973), `pymoogi`, `scipy` (Virtanen et al. 2019), `numpy` (van der Walt et al. 2011), `matplotlib` (Hunter 2007), `emcee` (Foreman-Mackey et al. 2013), `UVW calculator` (https://github.com/dr-rodriguez/UVW_Calculator).

ORCID iDs

Z. G. Maas https://orcid.org/0000-0002-0475-3662
G. Cescutti https://orcid.org/0000-0002-3184-9918
C. A. Pilachowski https://orcid.org/0000-0002-3007-206X

References

Afşar, M., Sneden, C., Wood, M. P., et al. 2018, ApJ, 865, 44
Asplund, M., Grevesse, N., Sauval, A. J., & Scott, P. 2009, ARA&A, 47, 481
Bensby, T., Feltzing, S., & Oey, M. S. 2014, A&A, 562, A71
Berzinsh, U., Svanberg, S., & Biemont, E. 1997, A&A, 326, 412
Böcek Topcu, G., Afşar, M., Sneden, C., et al. 2019, MNRAS, 485, 4625
Caffau, E., Andrievsky, S., Korotin, S., et al. 2016, A&A, 585, A16
Caffau, E., Bonifacio, P., Faraggiana, R., & Steffen, M. 2011, A&A, 532, A98
Caffau, E., Bonifacio, P., Oliva, E., et al. 2019, A&A, 622, A68
Caffau, E., Steffen, M., Sbordone, L., Ludwig, H.-G., & Bonifacio, P. 2007, A&A, 473, L9
Carrera, R., & Pancino, E. 2011, A&A, 535, A30
Cescutti, G., Matteucci, F., Caffau, E., & François, P. 2012, A&A, 540, A33
de Bruijne, J. H. J., Hoogerwerf, R., & de Zeeuw, P. T. 2001, A&A, 367, 111
Dutra-Ferreira, L., Pasquini, L., Smiljanic, R., Porto de Mello, G. F., & Steffen, M. 2016, A&A, 585, A75
ESA 1997, The Hipparcos and Tycho catalogues. Astrometric and photometric star catalogues derived from the ESA Hipparcos Space Astrometry Mission (Noordwijk: ESA)
Feuillet, D. K., Bovy, J., Holtzman, J., et al. 2018, MNRAS, 477, 2326
Foreman-Mackey, D., Hogg, D. W., Lang, D., & Goodman, J. 2013, PASP, 125, 306
François, P., Matteucci, F., Cayrel, R., et al. 2004, A&A, 421, 613
Gaia Collaboration, Brown, A. G. A., Vallenari, A., et al. 2018, A&A, 616, A1
Gehren, T., Shi, J. R., Zhang, H. W., Zhao, G., & Korn, A. J. 2006, A&A, 451, 1065
González Hernández, J. I., & Bonifacio, P. 2009, A&A, 497, 497
Gustafsson, B., Edvardsson, B., Eriksson, K., et al. 2008, A&A, 486, 951
Hasselquist, S., Shetrone, M., Smith, V., et al. 2017, ApJ, 845, 162
Hawkins, K., Masseron, T., Jofré, P., et al. 2016, A&A, 594, A43
Hinkel, N. R., Mamajek, E. E., Turnbull, M. C., et al. 2017, ApJ, 848, 34
Hinkle, K. H., Cuberly, R., Gaughan, N., et al. 1998, Proc. SPIE, 3354, 810
Holmberg, J., Nordström, B., & Andersen, J. 2009, A&A, 501, 941
Holtzman, J. A., Hasselquist, S., Shetrone, M., et al. 2018, AJ, 156, 125
Hunter, J. D. 2007, CSE, 9, 90
Jacobson, H. R., Thanathibodee, T., Frebel, A., et al. 2014, ApJL, 796, L24
Jönsson, H., Allende Prieto, C., Holtzman, J. A., et al. 2018, AJ, 156, 126
Karakas, A. I., & Lugaro, M. 2016, ApJ, 825, 26
Kobayashi, C., Karakas, A. I., & Umeda, H. 2011, MNRAS, 414, 3231
Kobayashi, C., Umeda, H., Nomoto, K., Tominaga, N., & Ohkubo, T. 2006, ApJ, 653, 1145
Leung, S.-C., & Nomoto, K. 2018, ApJ, 861, 143
Limongi, M., & Chieffi, A. 2018, ApJS, 237, 13
Maas, Z. G., Pilachowski, C. A., & Cescutti, G. 2017, ApJ, 841, 108
Perryman, M. A. C., Brown, A. G. A., Lebreton, Y., et al. 1998, A&A, 331, 81
Prantzos, N., Abia, C., Limongi, M., et al. 2018, MNRAS, 476, 3432
Ramírez, I., & Allende Prieto, C. 2011, ApJ, 743, 135
Ramírez, I., Allende Prieto, C., & Lambert, D. L. 2013, ApJ, 764, 78
Ramírez, I., Meléndez, J., Bean, J., et al. 2014, A&A, 572, A48
Reddy, B. E., Tomkin, J., Lambert, D. L., et al. 2003, MNRAS, 340, 304
Ritter, C., Andrassy, R., Côté, B., et al. 2018, MNRAS, 474, L1
Roederer, I. U., Jacobson, H. R., Thanathibodee, T., Frebel, A., & Toller, E. 2014, ApJ, 797, 69
Silva Aguirre, V., Bojsen-Hansen, M., Slumstrup, D., et al. 2018, MNRAS, 475, 5487
Skrutskie, M. F., Cutri, R. M., Stiening, R., et al. 2006, AJ, 131, 1163
Sneden, C. 1973, ApJ, 184, 839
Spite, M., Peterson, R. C., Gallagher, A. J., Barbuy, B., & Spite, F. 2017, A&A, 600, A26
Takeda, Y., Honda, S., Ohnishi, T., et al. 2013, PASJ, 65, 53
Tody, D. 1986, Proc. SPIE, 627, 733
Tody, D. 1993, ASP Conf. Ser. 52, Astronomical Data Analysis Software and Systems II, ed. R. J. Hanisch, R. V. J. Brissenden, & J. Barnes, (San Francisco, CA: ASP), 173
Travaglio, C., Hillebrandt, W., Reinecke, M., & Thielemann, F.-K. 2004, A&A, 425, 1029
van der Walt, S., Colbert, S. C., & Varoquaux, G. 2011, CSE, 13, 22
van Leeuwen, F. 2007, A&A, 474, 653
Virtanen, P., Gommers, R., & Oliphant, T. E. 2019, arXiv:1907.10121
Weinberg, D. H., Holtzman, J. A., Hasselquist, S., et al. 2019, ApJ, 874, 102
Woosley, S. E., & Weaver, T. A. 1995, ApJS, 101, 181
Yi, S., Demarque, P., Kim, Y.-C., et al. 2001, ApJS, 136, 417